IOP Conference Series: Materials Science and Engineering

Meshless simulation of a macrosegregation benchmark considering the solid motion

Meshless simulation of a macrosegregation benchmark considering the solid motion

Viktor Govže[1], Igor Vušanović[2] and Božidar Šarler[1,3,*]

[1] Institute of Metals and Technology, Ljubljana, Slovenia
[2] Faculty of Mechanical Engineering, University of Montenegro, Podgorica, Montenegro
[3] Faculty of Mechanical Engineering, University of Ljubljana, Ljubljana, Slovenia

E-mail: viktor.govze@imt.si, igorvus@ucg.ac.me, *bozidar.sarler@fs.uni-lj.si

Abstract. We have extended the existing two-dimensional rigid solid phase benchmark for binary substance with the solid phase motion in the present paper. Incompressible laminar Newtonian flow is assumed, and a standard mixture formulation is used for the mass, momentum, energy, and solute transport. A coherency solid motion model accounts for the free-floating grains, assuming that the solid velocity is proportional to the mixture velocity and the liquid fraction. The lever rule is used to describe the mass fractions of the phases. A two-dimensional benchmark is solved using the semi-implicit meshless diffuse approximate method with an adaptive subdomain upwinding strategy. The results of the meshless method are compared to the finite volume method results with a reasonable agreement. The new benchmark results show that the solid motion has an essential effect on the macrosegregation pattern.

1. Introduction

The incorporation of the movement of free-floating grains into solidification simulation results in improved fidelity of the results. For example, it was observed that the solid motion might cause inverse segregation in the billet centre during the direct chill casting of aluminium alloys [1]. Several benchmark cases were proposed in [2] to test and verify the implementations of the solidification models. In the present paper, we aim to extend one of the proposed benchmarks with a model considering the solid motion on a reduced scale, like in [3]. So far, different models for treating free-floating grains were developed, which differ in complexity. For example, in [4], a two-region approach has been developed, which divides the solidification region into the slurry and the rigid region. In the slurry region, the solid is allowed to move with the convective currents, and in the rigid region, it is assumed to behave as a rigid structure, with a critical solid fraction being the slurry-mushy partitioning parameter. More recently, an attempt to reduce the complexity of such models was presented [5]. This enables to include the solid motion in the existing mixture continuum equations developed in the eighties [6]. In the present benchmark, a simple non-parametric coherency solid motion model is used, which assumes that the solid velocity is proportional to the mixture velocity through the liquid fraction. Previously, the benchmark with the solid motion model, based on the rigid solid assumption, was successfully solved with different strong-form meshless methods [3, 7]. In the present extended benchmark, the diffuse approximate method (DAM) is used to obtain the numerical solution, and the results are compared to the finite volume method (FVM) with reasonable agreement.

2. Problem definition

The physical model is derived based on the mixture continuum assumption for a multi-component substance elaborated in [6]. The coupled mass, energy, species, and momentum conservation equations are formulated for an incompressible Newtonian fluid. The solidification process of a binary alloy is considered, and the lever rule is used for the mass fractions of the phases. A linearized binary phase diagram is used to describe the local equilibrium conditions.

The governing equations describing the macroscopic model are given as

$$\nabla \cdot \mathbf{v} = 0, \tag{1}$$

$$\rho \frac{\partial h}{\partial t} + \rho \left(\mathbf{v} \cdot \nabla\right) h = k \nabla^2 T - \rho \nabla \cdot \left[\left(h_l - h\right)\left(\mathbf{v} - \mathbf{v_s}\right)\right], \tag{2}$$

$$\frac{\partial C}{\partial t} + \left(\mathbf{v} \cdot \nabla\right) C = -\nabla \cdot \left[\left(C_l - C\right)\left(\mathbf{v} - \mathbf{v_s}\right)\right], \tag{3}$$

$$\rho \frac{\partial \mathbf{v}}{\partial t} + \rho \left(\mathbf{v} \cdot \nabla\right) \mathbf{v} = -\nabla p + \mu \nabla^2 \mathbf{v} + \mathbf{b}_D + \mathbf{b}_B, \tag{4}$$

where ρ, $\mathbf{v}$, h, k and C are the mixture density, velocity, enthalpy, thermal conductivity, and species concentration, μ is the liquid viscosity, T is the temperature, and p is the pressure. The individual phase variables are denoted with indexes l for liquid and s for solid, therefore h_l is the liquid enthalpy, C_l is the liquid species concentration, and $\mathbf{v}_s$ is the solid velocity. The additional body forces $\mathbf{b}_D$ and $\mathbf{b}_B$ exerted on the mixture are the hydraulic drag force in the solidifying region modelled with Darcy law and the buoyancy force modelled with the Boussinesq approximation. Their definitions are

$$\mathbf{b}_D = -\frac{\mu}{K}\left(\mathbf{v} - \mathbf{v}_s\right), \tag{5}$$

$$\mathbf{b}_B = \rho_{ref}\left[1 - \beta_T\left(T - T_{ref}\right) - \beta_C\left(C_l - C_{ref}\right)\right]\mathbf{g}, \tag{6}$$

where K is the isotropic hydraulic permeability, ρ_{ref}, T_{ref}, and C_{ref} represent the reference density, temperature and species concentration, β_T and β_C are the thermal and species volumetric expansion coefficient, and $\mathbf{g}$ is the gravitational acceleration. The hydraulic permeability is modelled with the Carman-Kozeny relation, defined as

$$K = K_0 \frac{g_l^3}{\left(1 - g_l\right)^2}, \tag{7}$$

where K_0 is the Kozeny constant and g is the volumetric fraction. The mixture quantities are defined as

$$\mathbf{v} = g_l \mathbf{v}_l + g_s \mathbf{v}_s, \tag{8}$$

$$h = c_p T + g_l L, \tag{9}$$

$$C = \left[g_l + \left(1 - g_l\right) k_p\right] C_l, \tag{10}$$

where c_p is the mass specific heat at a constant pressure of the liquid and the solid phase, L is the latent heat, and k_p is the partition coefficient. The equilibrium liquidus temperature T_{liq} is defined as

$$T_{liq} = T_f + m C_l, \tag{11}$$

where T_f is the pure substance temperature of fusion and m is the slope of the liquidus line.

In the present paper, we compare the results of the rigid and the coherency solid motion models. The former is defined as

$$\mathbf{v}_s = \mathbf{v}_{sys}, \tag{12}$$

where $\mathbf{v}_{sys}$ is the velocity of the system, and the latter is defined as

$$\mathbf{v}_s = g_l \mathbf{v} + (1 - g_l)\mathbf{v}_{sys}, \tag{13}$$

where the liquid and solid fractions measure the intensity of the solid phase movement. In the present article, $\mathbf{v}_{sys} = \mathbf{0}\ \mathrm{m\,s^{-1}}$, since the system is stationary.

The problem geometry is shown in figure 1 together with the mathematical description of the boundary conditions, initial conditions, and the reference points with cross-sections used in the analysis of the results in tables 1-3.

A two-dimensional cartesian coordinate frame with basis vectors $\mathbf{i}_x$ and $\mathbf{i}_y$ and the position vector $\mathbf{p} = x\mathbf{i}_x + y\mathbf{i}_y$ is used to describe the problem. Points A, B, C and D define the corner points of the rectangular cavity and segments AB, BC, CD, and AD represent the boundaries of the cavity. The boundary is denoted with Γ and the interior is denoted with Ω.

The problem is symmetric about the left boundary. The cavity is impermeable for species transfer on the top, right, and bottom and thermally insulated at the top and bottom. Heat is extracted from the right boundary through forced convection with a heat transfer coefficient $\tilde{h}$ to the surroundings with temperature T_{env}. A sticking boundary condition is used on all non-symmetry boundaries. Initially, the melt is at rest with the temperature and the species concentration uniformly distributed and set to T_0 and C_0. The numerical values of the parameters used in the simulation are given in table 4.

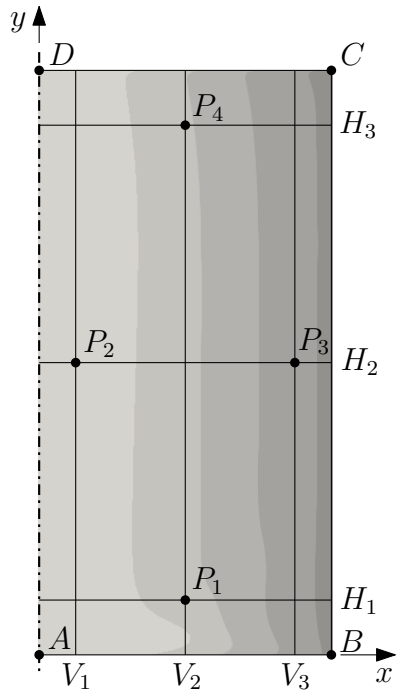

Figure 1: The solidifying domain.

Table 1: The reference points.

		A	B	C	D	P_1	P_2	P_3	P_4
x	[mm]	0	10	10	0	5	1	9	5
y	[mm]	0	0	20	20	2	10	10	18

Table 2: The cross sections.

		H_1	H_2	H_3	V_1	V_2	V_3
x	[mm]	x	x	x	P_2	P_1	P_3
y	[mm]	P_1	P_2	P_4	y	y	y

Table 3: The boundary and initial conditions.

$\mathbf{p} \in \Gamma_{AB}, t > 0$ s
$C = C_0$, $\mathbf{v} = \mathbf{v}_{sys}$, $\frac{dT}{d\mathbf{n}} = 0\ \mathrm{K\,m^{-1}}$

$\mathbf{p} \in \Gamma_{BC}, t > 0$ s
$C = C_0$, $\mathbf{v} = \mathbf{v}_{sys}$, $\frac{dT}{d\mathbf{n}} = \tilde{h}\,(T - T_{env})$

$\mathbf{p} \in \Gamma_{CD}, t > 0$ s
$C = C_0$, $\mathbf{v} = \mathbf{v}_{sys}$, $\frac{dT}{d\mathbf{n}} = 0\ \mathrm{K\,m^{-1}}$

$\mathbf{p} \in \Gamma_{DA}, t > 0$ s
$\frac{dC}{d\mathbf{n}} = 0\ \mathrm{m^{-1}}$, $v_x = 0\ \mathrm{m\,s^{-1}}$, $\frac{dv_y}{d\mathbf{n}} = 0\ \mathrm{s^{-1}}$, $\frac{dT}{d\mathbf{n}} = 0\ \mathrm{K\,m^{-1}}$

$\mathbf{p} \in \Omega, t = 0$ s
$C = C_0$, $\mathbf{v} = \mathbf{v}_{sys}$, $T = T_0$

3. Solution procedure

The solution to the problem stated is calculated by using DAM, which belongs to local strong-form meshless methods. This method uses weighted least squares to determine a locally smooth solution and has been used to solve several solidification problems before [8, 7, 9, 10]. The shape functions Ψ_k used in this work are Gaussian function weighted monomials defined as

$$\Psi_k(\mathbf{r}) = \mathrm{e}^{-W\left(\frac{\|\mathbf{r}\|}{D}\right)^2} \psi_k\left(\frac{\mathbf{r}}{D}\right), \qquad \mathbf{r} = \mathbf{p} - \mathbf{p}_0, \quad (14)$$

where W is the Gaussian weighting function sharpness parameter, $\|\cdot\|$ represents the Euclidian norm, $\mathbf{r}$ represents the relative position vector, D is a normalization constant, ψ_k is the k-th monomial from the set of monomials $\left\{1, r_x, r_y, r_x^2, r_y^2, r_x r_y\right\}$, and $\mathbf{p}_0$ is the position of the node of interest.

The governing equations are propagated through time by using a first-order accurate scheme. The energy (2) and species (3) equation are solved in a fully explicit manner, whilst the momentum equation is solved in a semi-implicit manner.

Table 4: Thermophysical parameters.

ρ	2450	$\mathrm{kg\,m^{-3}}$
c_p	1000	$\mathrm{J\,kg^{-1}\,K^{-1}}$
k	192	$\mathrm{W\,m^{-1}\,K^{-1}}$
L	4×10^5	$\mathrm{J\,kg^{-1}}$
μ	1.2×10^{-3}	$\mathrm{Pa\,s}$
β_T	1.3×10^{-4}	$\mathrm{K^{-1}}$
β_C	-7.3×10^{-3}	$\mathrm{wt\%^{-1}}$
ρ_{ref}	2450	$\mathrm{kg\,m^{-3}}$
T_{ref}	465	°C
C_{ref}	4.5	wt%
$\mathbf{g}$	$-9.8\mathbf{i}_y$	$\mathrm{m\,s^{-2}}$
K_0	5.56×10^{-11}	$\mathrm{m^2}$
T_f	660	°C
m	-3.43	$\mathrm{°C\,wt\%^{-1}}$
k_p	0.173	/
$\tilde{h}$	500	$\mathrm{W\,m^{-2}\,K^{-1}}$
T_{env}	20	°C
T_0	700	°C
C_0	4.5	wt%
$\mathbf{v}_{sys}$	$\mathbf{0}$	$\mathrm{m\,s^{-1}}$

During solidification, the Darcy term (5) in the mixture momentum equation poses a serious numerical stability issue if a fully explicit approach is used. For this reason, the part of the Darcy term associated with the mixture velocity is treated implicitly. To avoid singularity when the liquid fraction approaches 0, the permeability is calculated up to a small liquid fraction ϵ and $K(g_l = \epsilon)$ is used at $g_l < \epsilon$. In this way, no error is introduced in the permeability calculation when $g_l \geq \epsilon$. In the present paper, $\epsilon = 1 \times 10^{-2}$, where the Darcy drag force is practically infinite and the mixture is stationary.

The momentum and continuity equations are directly coupled to satisfy the discrete incompressibility constraint exactly. To prevent numerical instabilities resulting from the advective terms in the governing equations, an upwinding stabilization method is used similar to the one in [11].

The support subdomains include $N_{loc} = 9$ nearest nodes and the chosen Gaussian weighting parameter is $W = 5$. The normalization constant is defined as

$$D = \max\left(\|\mathbf{r}_j\|\right), \qquad j = 1, \ldots, N_{loc}, \quad (15)$$

where j represents the local node index. The time step is $\Delta t = 4 \times 10^{-5}$ s. To test the convergence of the solution, grids of 20×40, 25×50, 40×80, 50×100, and 80×160 nodes were used with the same time step and numerical parameters. The meshless simulation is performed on an Intel Xeon Gold 6146 CPU and is parallelized to use 6 cores. The wall time of the simulation run for the 80×160 set of nodes was 34 h.

The reference results are calculated using FVM. The momentum equation is solved in a fully implicit manner and the pressure-velocity coupling is made with the SIMPLE algorithm as proposed by Patankar (1980). The energy and species concentration equations are solved in a fully explicit manner. The advection terms are treated by a first-order upwinding stabilization method. The results shown are calculated on a regular 80×160 mesh with the time step $\Delta t = 8 \times 10^{-6}$ s.

4. Results

As can be seen in the comparison of the final macrosegregation in figure 2, very different results are obtained just by using a different solid velocity constitutive relation. Since the species transport is governed exclusively by advection in both models, whatever influences the mixture velocity will also influence the final macrosegregation. Compared to the rigid model, the species concentration is more evenly distributed throughout the cavity when using the coherency model. Even though its peak is still at the bottom, it is significantly lower than in the rigid model. The convergence of the solutions is monitored in terms of the species concentration field standard deviation and the minimum and maximum absolute value of segregation $S_{\min\,|\,\max}$ defined as

$$\mathrm{std}\,(C) = \sqrt{\frac{1}{N-1}\sum_{n=1}^{N}\left(C\left(\mathbf{p}_n\right) - C_0\right)}, \quad S_{\min\,|\,\max} = \min\,|\,\max\left(\left|C\left(\mathbf{p}_n\right) - C_0\right|\right), \quad n = 1, \ldots, N, \tag{16}$$

where N is the number of nodes used in the simulation. The convergence is measured against the relative grid spacing. For both the rigid and the coherency model, the convergence of the chosen parameters is shown in figure 3.

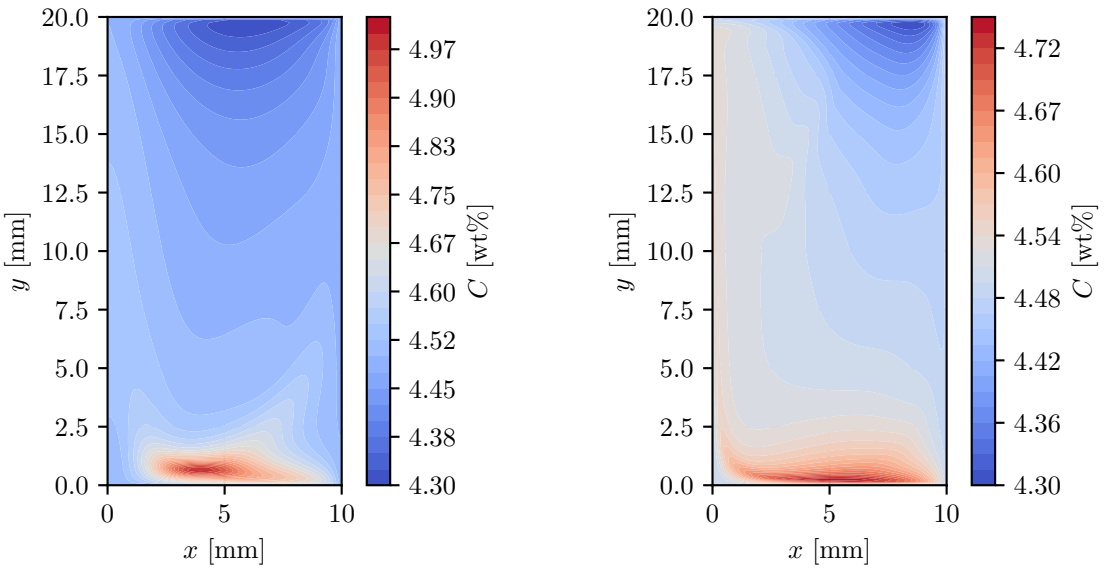

Figure 2: Macrosegregation comparison of the DAM solutions of the (a) rigid and the (b) coherency model.

Even though a relatively fine regular grid of nodes is used, the solution is still underresolved in the vicinity of the boundaries for the coherency model both in the FVM and DAM solutions of the problem. Compared to the rigid model's solution, the coherency model's solution exhibits sharper species concentration peaks, which require a dense node arrangement to be properly resolved. Even more nodes than used would be required, especially near the boundaries, which is impractical to do with a regular grid node arrangement. A node set biased towards the boundaries of the cavity would be better suited. The results converge slower than the rigid model results but are nevertheless slowly convergent concerning std(C). A parametric study with denser node arrangements would have to be used to determine more accurate results.

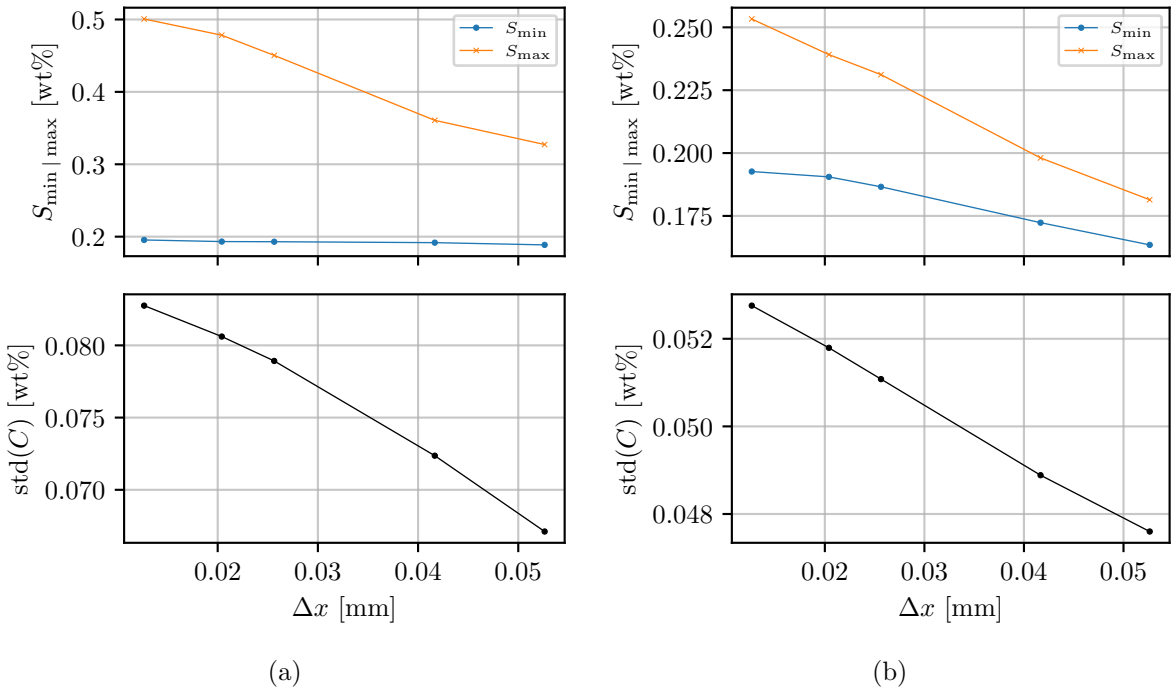

Figure 3: DAM solutions convergence for (a) rigid and (b) coherency model.

Practically speaking, the macrosegregation on the 80×160 node arrangement yields a very similar solution as the 40×80, and the trend is unlikely to change with denser nodes.

To analyze the results more thoroughly, horizontal and vertical cross-section results are provided in figure 4. The DAM solution of the rigid model was verified using the results presented in [3] and the comparison is for clarity not shown in the figure. A qualitative agreement between the results of the FVM and DAM is obtained. One can attribute the quantitative disagreement to the first-order upwind method in FVM, which is known to introduce numerical diffusion. In the meshless solution procedure, the upwinding method is analogous to the second-order finite difference upwinding method, and therefore, less numerical diffusion is introduced as in FVM solution.

From the time evolution of the magnitude of the mixture velocity for each of the reference points in figure 5a the mixture velocity in the coherency model is equal to or larger than its rigid counterpart. That is because the moving solid incorporated through the coherency model imposes less drag on the mixture flow in the solidification region than the rigid model. The coherency model progressively builds up the drag by a factor of $1 - g_l$ since $\mathbf{v}_{sys} = \mathbf{0}\ \mathrm{m\,s^{-1}}$. As a result, the flow is faster in the solidifying region allowing for more solute advection. Consequently, this leads to more evenly distributed macrosegregation, as seen in figure 2b.

Both models are similar in terms of the solidification start and end times, which are at 5 s and 45 s, respectively. As expected, both models behave the same in the fully liquid region but quite differently during the solidification. The time it takes for the macrosegregation to appear like the final macrosegregation is very different. In the rigid model, it takes 4 s after the solidification start, whilst in the coherency model, it takes 12 s. This can be attributed to the flow being less constrained in the slurry, allowing the solute to be more freely distributed, resulting in changing species concentration field. This effect can be more clearly seen in figure 5b, where a small peak in species concentration is reached in P_2 before decreasing and increasing again. The temperature distribution remains approximately the same, since the maximum local Péclet

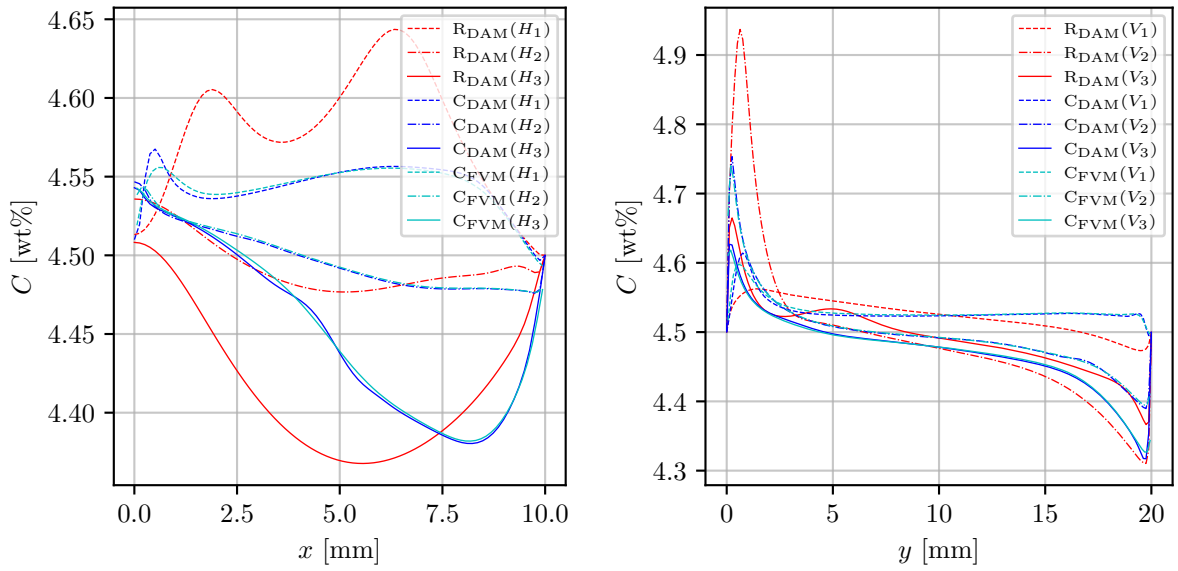

(a) (b)

Figure 4: A comparison of the solution of the rigid (denoted as R) and the coherency (denoted as C) models with DAM and FVM. Horizontal (a) and vertical (b) cross section.

number is on the order of magnitude of 2×10^{-1} and the diffusive heat transport dominates in the energy transport equation.

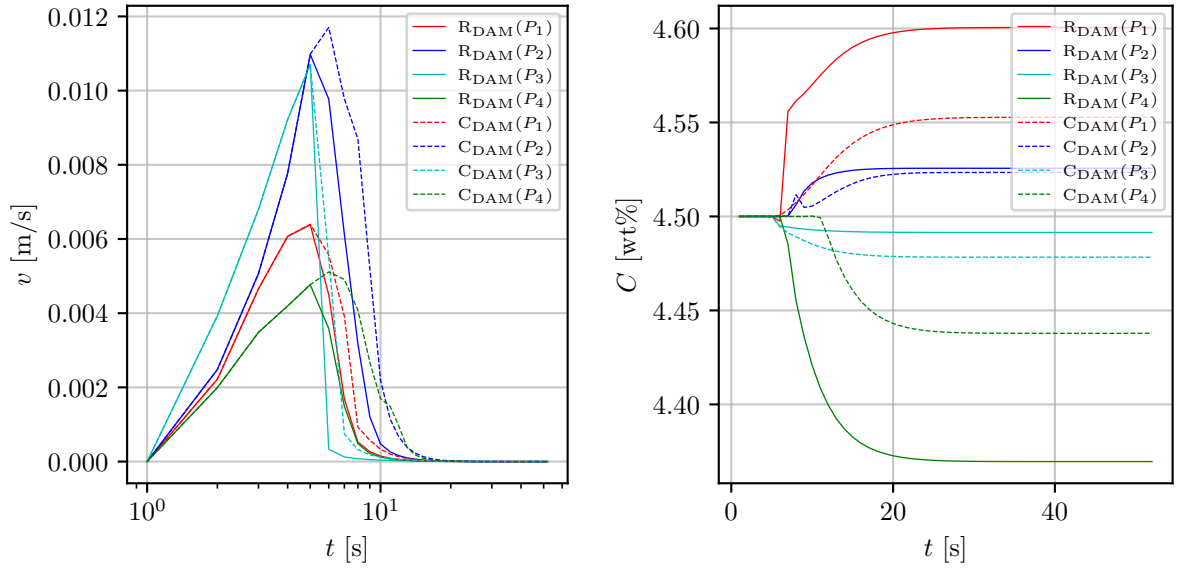

(a) (b)

Figure 5: Concentration and velocity magnitude at the reference points for the rigid (denoted as R) and the coherency (denoted as C) models of a meshless DAM solution.

5. Conclusion

In the present paper, the macrosegregation benchmark [3] has been extended to consider the solid motion through a simple coherency model, and the results were compared to the original benchmark case. Different numerical approaches, namely the DAM and FVM have been used to implement the physical model, and a qualitative agreement was reached between the two methods. The elaboration of the meshless solution procedure will be presented in a follow-up publication. Convergence of the results of the meshless method is shown where it can be seen that DAM can be used to get accurate predictions of the macrosegregation. The effect of the solid motion model is demonstrated, producing significantly different results than the rigid model case.

Acknowledgments

This work was supported by the Slovenian Research Agency (grant numbers J2-4477, P2-0162) and bilateral Slovenian-Montenegrin project (grant number BI-ME/23-24-009).

References

[1] Nadella R, Eskin D G, Du Q and Katgerman L **53** 421–480 ISSN 0079-6425 URL https://www.sciencedirect.com/science/article/pii/S007964250700059X
[2] Bellet M, Combeau H, Fautrelle Y, Gobin D, Rady M, Arquis E, Budenkova O, Dussoubs B, Duterrail Y, Kumar A, Gandin C, Goyeau B, Mosbah S and Založnik M **48** 2013–2016 ISSN 12900729 URL https://linkinghub.elsevier.com/retrieve/pii/S129007290900177X
[3] Kosec G, Založnik M, Šarler B and Combeau H **22**(2) 169–196 ISSN 1546-2218, 1546-2218 URL https://www.techscience.com/cmc/v22n2/22619
[4] Ni J and Incropera F P **38** 1285–1296 ISSN 0017-9310 URL https://www.sciencedirect.com/science/article/pii/001793109400237P
[5] Vušanović I and Voller V **169** 120923 ISSN 00179310 URL https://linkinghub.elsevier.com/retrieve/pii/S0017931021000260
[6] Bennon W D and Incropera F P **30** 2161–2170 ISSN 0017-9310 URL https://www.sciencedirect.com/science/article/pii/0017931087900949
[7] Hatić V, Mavrič B and Šarler B **28** 361–380 ISSN 0961-5539 URL https://www.emerald.com/insight/content/doi/10.1108/HFF-04-2017-0143/full/html
[8] Hatić V, Mavrič B, Košnik N and Šarler B **54** 170–188 ISSN 0307904X URL https://linkinghub.elsevier.com/retrieve/pii/S0307904X17305863
[9] Hatić V, Cisternas Fernández M, Mavrič B, Založnik M, Combeau H and Šarler B **142** 121–133 ISSN 12900729 URL https://linkinghub.elsevier.com/retrieve/pii/S1290072918319197
[10] Hatič V, Mavrič B and Šarler B **113** 191–203 ISSN 09557997 URL https://linkinghub.elsevier.com/retrieve/pii/S0955799719306678
[11] Chan Y, Shen L, Wu C and Young D **89** 157–166 ISSN 00457930 URL https://linkinghub.elsevier.com/retrieve/pii/S0045793013004155